MASTER'S THESIS

Open-Channel Flow Over Naturally Rough Surfaces

A CFD Study

Anton Burman
2016

Master of Science in Engineering Technology
Engineering Physics and Electrical Engineering

Luleå University of Technology
Department of Engineering Scienes and Mathematics

LULEÅ UNIVERSITY OF TECHNOLOGY

Abstract

In proximity to hydropower plants the watercourses usually vary substantially in channel bed topography, this means that stochastic large-scale roughness elements are apparent. The water level in the watercourses also vary heavily as a function of how much electricity that is being produced by the plant. This in turn can be troublesome for local fauna and flora. At Vattenfall Research and Development in Älvkarleby a channel aimed to emulate such watercourses has been built. The aim of this thesis is to gain further insight in flow phenomena as a function of the roughness and the water level by doing CFD simulations on the channel in Älvkarleby. In this work several contours for different water levels have been provided as well as double-averaged velocity profiles. Additionally the Gauckler-Manning Coefficient have been evaluated for all water levels. Furthermore the turbulent energy spectra is provided as a function of the water depth. The roughness was found to heavily contribute to the shape of the velocity field as well as the shape of the energy spectra. The work put forward in this thesis also highlights the need to properly resolve natural roughness in CFD and engineering applications.

PREFACE

This work has been performed at the division of Fluid and Experimental Mechanics at Luleå University of Technology. First and foremost I would like to thank my supervisor Dr. Gunnar Hellström for all his help during this work. I would also like to thank adjunct Professor Patrik Andreasson for all his help and encouragement. I also want to thank PHD-student Robin Andersson for his insight and help with this project. Additionally I would also like to thank all the friendly people at the division for creating such a nice working environment. Finally I want to thank my family for always being supportive throughout my education.

Anton Burman
Luleå, June 2016

NOMENCLATURE

η	Kolmogorov lengthscale $[m]$
$\frac{\overline{D}}{\overline{Dt}}$	Mean-substantial derivative
κ	Wavenumber $[1/m]$
$\langle\tilde{\boldsymbol{u}}(\boldsymbol{x},t)\rangle$	Double-averaged velocity $[m/s]$
A_c	Cross section area $[m^2]$
D_H	Hydraulic diameter $[m]$
f	Friction factor [1]
GCI_{fine}	Fine-grid convergence index
H	Depth of water surface $[m]$
n	Gauckler-Manning Coefficient $[s/m^{1/3}]$
P_w	Wetted perimeter $[m]$
R_H	Hydraulic Radius $[m]$
y^+	Dimensionless wall distance [1]

Contents

CHAPTER 1

Introduction

1.1 Background Hydropower

Hydropower is together with nuclear power the biggest producer of electricity in Sweden. In 2014 approximately 40% of Sweden's entire electricity production was produced by hydropower [1]. One of the perks with hydropower is the possibility to effectively store potential energy in the form of water in a reservoir. By doing this the plant can then produce electricity when the demand is high. This in turn can be troublesome for environmental reasons, the variations in water level give rise to different shear stresses along the bed, this can be problematic for local fauna and migratory fish species such as salmon or trout [2]. In order to protect water quality and biological diversity the European Union introduced the EU Water Framework Directive [3]. As of December 2000 all member states of the European Union must adhere to the EU Water Framework Directive. In proximity of hydropower plants there are watercourses that have varying water depth depending on how much electricity is being produced at that particular time. These waterways are often man made channels, for instance spillways, or the remnants of some old river bed. In general these channels vary heavily in topography. The flow under these conditions is always turbulent and exposed to the atmosphere.

1.2 Previous Work

Turbulent flow over rough surfaces is hardly something new in the field of fluid mechanics. Traditionally in engineering applications methods using uniform roughness, i.e Darcy friction factor and its derivatives have been used. With the advancement of modern computing high resolution simulations have been used in more fundamental research. Direct numerical simulations have been used on wavy surfaces [4] and square ribs [5] to gain further insight into roughness related flow phenomena. Unfortunately direct numerical simulations are not realistic to use in engineering applications or hydropower

related research at the time of this thesis. Previous and on-going research at Luleå University of Technology highlights the importance of resolving the wall-roughness rather than using a uniform roughness model and sub-grid methods [6].

1.3 Problem Formulation and Aim of the Thesis

At Vattenfall Research and Development in Älvkarleby a channel with rough walls has been built as a pure CFD validation channel. The actual channel can be seen in figure 1.1. The channel is 0.7 m high, 1.2 m wide and 24 m long. The roughness of the wall has been generated with a fractal algorithm. The goal of this thesis is to find a working CFD-model of the channel. Once this has been established additional parameters related to the roughness of the channel can be evaulated, i.e the Gauckler-Mannings number. Furthermore are turbulent properties and the relationship to the water levels and the roughness of additional interest. Due to limits in computational power only a part of the channel will be used.

Figure 1.1: Open-channel with rough walls at Vattenfall Research and Development in Älvkarleby.

CHAPTER 2

Theory

2.1 Fluid Mechanics - Governing Equations

Fluid Mechanics is the study of how *fluids* behaves when subject to forces. In general the forces are split into two categories, *body* and *surface* forces, an example of a body force is the gravitational force, an example of a surface force is for instance shear forces caused by the wind blowing [7]. The equations governing the fluid motions are the Navier-Stokes equations (2.1) and the continuity equation (2.2)

$$\frac{\partial \boldsymbol{u}}{\partial t} + (\boldsymbol{u} \cdot \nabla)\boldsymbol{u} = -\frac{1}{\rho}\nabla p + \boldsymbol{F} + \frac{\mu}{\rho}\nabla^2 \boldsymbol{u} \tag{2.1}$$

$$\nabla \cdot \boldsymbol{u} = 0 \tag{2.2}$$

where ρ is the density of the fluid, $\boldsymbol{u}$ is the velocity vector, p is the total pressure, $\boldsymbol{F}$ is the sum of the body forces and μ is the dynamic viscosity of the fluid. The Navier-Stokes equations are derived from the principle of conservation of momentum, the continuity equation is derived from the principle of conservation of mass.

2.2 Turbulence

In Fluid Mechanics there are several dimensionless variables that relates to different flow properties. One such number is the Reynolds number

$$Re = \frac{\rho u L}{\mu} \tag{2.3}$$

where u is some representative velocity of the flow, for instance the bulk flow and L is some representative lengthscale for the flow. The Reynolds number is the ratio between inertial forces and viscous forces. The flow of the fluid can either be *laminar* or *turbulent*.

Whether the flow is laminar or turbulent is decided by the magnitude of the Reynolds number. For large Re the flow is turbulent, i.e when the inertial forces are comparatively large to the viscous forces. Laminar flow is characterized by smooth streamlines and highly ordered motion. Turbulent flow, on the other hand, is characterized by chaotic three-dimensional velocity fluctuations and highly disordered motion [8].

2.2.1 The Energy Cascade

A property of turbulent flow is the so called *turbulent energy cascade*. Kolmogorov hypothesized that the energy dissipation in turbulent flow is driven by different mechanisms at different lengthscales in the flow. At the largest lengthscales, energy dissipates from larger eddies into smaller eddies. Once the lengthscale of the eddies reaches the *Kolmogorov lengthscale* the energy is dissipated to heat via viscous deformation. The Kolmogorov lengthscale is defined as

$$\eta = \left(\frac{\nu^3}{\varepsilon}\right)^{1/4} \tag{2.4}$$

where ε is the rate of turbulent eddy dissipation. [9]

2.2.2 The Energy Spectra

A consequence of the Kolmogorov hypothesis is the turbulent energy spectrum. A model spectrum for the turbulent energy is

$$E(\kappa) = C\varepsilon^{2/3}\kappa^{-5/3} f_L(\kappa L) f_\eta(\kappa\eta) \tag{2.5}$$

where $C = 1.5$ is a model parameter and $\kappa = 2\pi/L$ is the wavenumber corresponding to the lengthscale L. The function $f_L(\kappa L)$ is modeled as

$$f_L = \left(\frac{\kappa L}{[(\kappa L)^2 + c_L]^{1/2}}\right)^{5/3+p_0} \tag{2.6}$$

where $p_0 = 2$. The function $f_\eta(\kappa\eta)$ is specified as

$$f_\eta(\kappa\eta) = exp(-\beta((\kappa\eta)^4 + c_\eta^4)^{1/4} - c_\eta) \tag{2.7}$$

where $\beta = 5.2$ is a model parameter. The variables $c_\eta \approx 0.4$ and and $c_L \approx 6.78$ are model parameters and are respectively decided by the normalization conditions

$$\int_\kappa E(\kappa) d\kappa = k \tag{2.8}$$

$$\int_{\kappa} 2\nu\kappa^2 E(\kappa) d\kappa = \varepsilon \tag{2.9}$$

respectively, where k is the turbulent kinetic energy. The Energy Spectrum Function (2.5) is not theoretically derived but rather tuned to satisfy fundamental turbulent properties such as proportionality to 5/3 in the inertial subrange [10].

2.2.3 Reynolds Averaged Navier-Stokes Equations

One common way to simplify the Navier-Stokes equations is to divide the velocity field into two parts, one mean component and one fluctuating random component

$$\boldsymbol{u}(\boldsymbol{x}, t) = \langle \boldsymbol{u}(\boldsymbol{x}, t) \rangle + \boldsymbol{u}'(\boldsymbol{x}, t) \tag{2.10}$$

where $\langle \boldsymbol{u}(\boldsymbol{x}, t) \rangle$ is the time-averaged velocity and $\boldsymbol{u}'(\boldsymbol{x}, t)$ are the turbulent fluctuations. This is called the *Reynolds decomposition*. From this decomposition the Reynolds-Averaged Navier-Stokes (RANS) equations follows. In tensor notation the equation can be written as

$$\frac{\overline{D}\langle U_j \rangle}{\overline{D}t} = \nu \nabla^2 \langle U_j \rangle - \frac{\partial \langle u_i u_j \rangle}{\partial x_i} - \frac{1}{\rho} \frac{\partial \langle p \rangle}{\partial x_j} \tag{2.11}$$

where $\frac{\overline{D}}{\overline{D}t}$ is the mean-substantial derivative, ν is the kinematic visocisty and $\frac{\partial \langle u_i u_j \rangle}{\partial x_i}$ is the derivative of the *Reynolds stress tensor*. The mean continuity equation is

$$\nabla \cdot \langle \boldsymbol{u}(\boldsymbol{x}, t) \rangle = 0. \tag{2.12}$$

Equations (2.11) and (2.12) together describe the three-dimensional time-averaged velocity field. There are four different equations and five unknown variables, three velocity components, the pressure and the Reynolds stress. This is known as a *closure problem*, in order to be able to solve the set of equations the Reynolds stress needs to be modeled [10].

2.3 Flow Over Rough Beds

2.3.1 Traditional Rough Wall Treatment

For sufficiently uniform rough surfaces the implicit equation known as the *Colebrook equation* can be used

$$\frac{1}{\sqrt{f}} = -2\log_{10}\left(\frac{\epsilon/D_H}{3.7} + \frac{2.51}{Re\sqrt{f}}\right). \tag{2.13}$$

where ϵ is the mean height of the roughness and D_H is the hydraulic diameter and f is the friction factor, also known as the Darcy friction factor. The ratio ϵ/D_H is also known as *equivalent sand-grain roughness* because the initial experiments designed

included surfaces where sand grains of known height had been glued to the walls [8]. By solving (2.13) for ϵ/D_H the explicit relation

$$\frac{\epsilon}{D_H} = 3.7\left(\frac{1}{10^{\frac{1}{2\sqrt{f}}}} - \frac{2.51}{Re\sqrt{f}}\right) \tag{2.14}$$

is obtained, see Appendix A for a derivation. The equivalent sand- grain method is implemented in ANSYS CFX, this model is however not suitable as an approximation for natural beds where the roughness is far from uniform.

2.3.2 Natural Roughness

In natural watercourses, rock excavated channels and tunnels or more or less any structure in nature the surfaces are characterized by chaotic non-uniform structures. One way of modeling these surfaces is by implementing some fractal algorithm that, given a flat surface, increases the complexity of that surface to a sufficient level. One of the most simple ways of generating such a topography is via the so called Diamond-Square algorithm.

The Diamond-Square Algorithm

The Diamond-Square algorithm randomly generates terrain contours using a Gaussian distribution. In figure 2.1 a schematic of how the algorithm works can be seen. The algorithm starts by dividing the surface into squares. Afterwards the algorithm computes the midpoint using the coordinates of the corners. The level of this midpoint is then computed using a Gaussian distribution where the standard deviation is based on the average level of the corners (black line in figure 2.1). Once this step of the algorithm is completed the next step is to compute a midpoint by using four new adjacent points (red line in figure 2.1) and so on until the geometry is sufficiently complex. In figure 2.1 two full iterations of the algorithm can be seen [11].

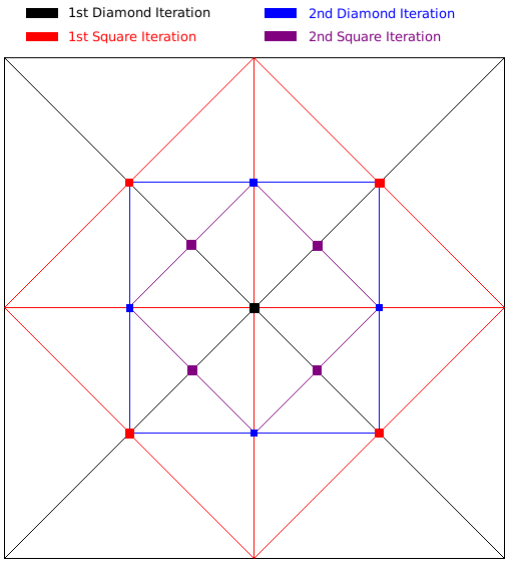

Figure 2.1: Schematic of the Diamond-Square algorithm.

2.3.3 Double-Averaged Navier-Stokes Equations

It has been suggested that for environmental hydraulics the conventional full roughness sub-grid representation approach is insufficient since the flow adjacent to the rough surface will always be non-uniform [12]. One way to combat this problem is to perform a so called double-averaging. Recall that the RANS equations are based upon time-averaging, with double-averaging one implies that the velocity components are averaged in both time and space. A decomposition similar to the Reynolds decomposition, called the Grays decomposition, can be used

$$\boldsymbol{u}(\boldsymbol{x},t) = \langle \tilde{\boldsymbol{u}}(\boldsymbol{x},t) \rangle + \overline{\boldsymbol{u}}(\boldsymbol{x},t) \tag{2.15}$$

where $\langle \tilde{\boldsymbol{u}}(\boldsymbol{x},t) \rangle$ is the double-averaged velocity and $\overline{\boldsymbol{u}}(\boldsymbol{x},t)$ are the spatial fluctuations. The double-averaged velocity is measured in a plane parallel to the mean flow. Averaging in space also introduces spatial fluctuations. These can statistically be modeled in a similar way as for the RANS equations. Unfortunately this feature is not implemented in ANSYS CFX. It has been suggested that spatial averaging can be done post simulation and still be meaningful [5].

2.4 Open-Channel Flow

Open-channel flow is a type of flow in a channel where a liquid is exposed to a gas. Most commonly the liquid is water that is exposed to atmospheric air. Typically the flow in

open channels is driven by gravity as opposed to pipe flow where the flow is often driven by pressure gradients [8].

2.4.1 Gauckler-Manning Coefficient

One way to quantitatively relate the surface roughness to the flow in open-channel flow is to use the Gauckler-Manning coefficient n. The Gauckler-Manning coefficient is assumed to be dependent only on the surface roughness. One way to derive an expression for the Gauckler-Manning coefficient is by using the friction slope S_f. The friction slope can be expressed as

$$S_f = \frac{f u_{mean}^2}{8 R_H g}. \tag{2.16}$$

The friction slope can alternatively be expressed as

$$S_f = \frac{n^2 u_{mean}^2}{R_H^{4/3}} \tag{2.17}$$

where R_H is the hydraulic radius, u_{mean} is the mean velocity, f is the friction factor and g is the gravitational acceleration. The hydraulic radius is defined as

$$R_H = \frac{A_c}{P_w} = 4 D_H \tag{2.18}$$

where A_c is the cross-section area, P_w is the wetted perimeter and D_H is the hydraulic diameter. By equating (2.16) with (2.17) and solving for n the following relation is obtained

$$n = \sqrt{\frac{f \sqrt[3]{R_H}}{4g}}. \tag{2.19}$$

The friction factor f can be expressed as

$$f = \frac{8\tau}{\rho u_{mean}^2} \tag{2.20}$$

where τ is the average wall stress and ρ is the density of water [8]. Substituting (2.20) into (2.19) yields

$$n = \sqrt{\frac{2\tau \sqrt[3]{R_H}}{\rho u_{mean}^2 g}}. \tag{2.21}$$

It's worth noting that the Gauckler-Manning coefficient is not dimensionless but has the dimension $[s/m^{1/3}]$ [13].

2.4.2 Froude Number

One important quantity in open-channel flow is the *Froude number*. The froude number is defined as

$$Fr = \frac{u_{mean}}{\sqrt{gL_c}} \tag{2.22}$$

where u_{mean} is the mean velocity at the cross-section, g is the gravitational acceleration and L_c is some characteristic lengthscale. For $Fr < 1$ the flow is *subcritical*, if $Fr = 1$ the flow is *critical* and if $Fr > 1$ the flow is *supercritical*. The Froude number describes in what direction a gravity wave on the surface travels. For subcritical flows the wave travels upstream but for supercritical flows the wave is swept away downstream, for critical flows the waves appear to be stationary. For supercritical flows hydraulic jumps may occur. The Froude number can be utilized for scaling when studying open-channel flows with different flow depths. If the Froude number is the same the flow is comparable [8][13].

2.5 CFD - Computational Fluid Dynamics

The Navier-Stokes equations are highly non-linear partial differential equations and can't be analytically solved for the general case. One way to combat this problem is to discretize the Navier-Stokes equations, using for instance the finite difference method or the finite volume method to get a system of algebraic equations instead. These systems of equations can then be solved by using numerical methods.

2.5.1 Errors in CFD

In CFD several different sources of errors arise naturally, they are; *model errors*, *discretization errrors* and *round-off errors*. Since the Navier-Stokes equations can't be solved for the general case some properties are often modeled, for instance turbulence. The results from these models will generally differ from the exact solution, this is what's referred to as the modeling errors. The discretization errors arise because there is a difference from the exact solution and the discretized system of equations. The solution might vary with the size of the system of equations (also called mesh), therefore it is important to investigate how the solution depends on the size of the mesh. Furthermore the round-off errors emerge from the fact that the computer can only represent a finite number of decimals [7] [14].

2.5.2 Richardson Extrapolation

One way to approximate the discretization error is by performing a so called Richardson extrapolation. First a representative mesh size needs to be defined

$$h = \left[\frac{1}{N}\sum_{i=1}^{N}(\Delta V_i)\right]^{1/3} \tag{2.23}$$

where N is the number of elements in the mesh and ΔV_i is the volume of an element. Then the apparent order of the method can be computed using equations (2.24)-(2.26)

$$p = \frac{1}{ln(r_{21})}\left|ln\left|\frac{\varepsilon_{32}}{\varepsilon_{21}}\right| + q(p)\right| \tag{2.24}$$

where

$$q(p) = ln\left(\frac{r_{21}^p - s}{r_{32}^p - s}\right) \tag{2.25}$$

and

$$s = sgn\left(\frac{\varepsilon_{32}}{\varepsilon_{21}}\right) \tag{2.26}$$

where sgn is the sign function, $\varepsilon_{32} = \Phi_3 - \Phi_2$, $\varepsilon_{21} = \Phi_2 - \Phi_1$ where Φ_j is some global parameter on the j-th mesh and $r_{32} = h_{coarse}/h_{fine}$. Equation (2.24) is an implicit equation, hence it needs to be solved iteratively. Once the apparent order is known the solution can be extrapolated with

$$\Phi_{ext}^{32} = \frac{r_{32}^p\Phi_2 - \Phi_3}{r_{32}^p - 1}. \tag{2.27}$$

Furthermore it's recommended that the following error estimates are reported: the approximate relative error, the extrapolated relative error and the fine-grid convergence index. The approximate relative error is defined as

$$e_a^{32} = \left|\frac{\Phi_2 - \Phi_3}{\Phi_2}\right| \tag{2.28}$$

analogously the extrapolated relative error is defined as

$$e_{ext}^{32} = \left|\frac{\Phi_{ext}^{32} - \Phi_2}{\Phi_{ext}^{32}}\right| \tag{2.29}$$

finally, the fine-grid convergence index is defined as

$$\mathrm{GCI}_{fine}^{32} = \frac{1.25e_a^{32}}{r_{32}^p - 1}. \tag{2.30}$$

The scheme is the same for any other indices of Φ [15].

2.5.3 Turbulence Modelling - The k-ε Model

There are several ways to model the Reynolds stress. Some commonly used methods are linear eddy viscosity models, algebraic models, one- and two-equation models and Reynold stress transport models (RSTM). The most commonly used turbulence model in industrial applications is the k-ε model. The k-ε model is based on the turbulent viscosity hypothesis. The k-ε model is a two equation model that models two turbulent quantities, the turbulent energy dissipation ε and the turbulent kinetic energy k. From these two quantities a turbulent time-scale (2.31), a turbulent lengthscale (2.32) and the turbulent viscosity (2.33) can be defined

$$T = \frac{k}{\varepsilon}, \tag{2.31}$$

$$L = \frac{k^{3/2}}{\varepsilon}, \tag{2.32}$$

$$\nu_T = \frac{C_\mu k^2}{\varepsilon}. \tag{2.33}$$

The transport equation for k is

$$\frac{\overline{D}k}{\overline{D}t} = \nabla \cdot \left(\frac{\nu_T}{\sigma_k} \nabla k \right) + P - \varepsilon. \tag{2.34}$$

Furthermore the equation for ε can be written as

$$\frac{\overline{D}\varepsilon}{\overline{D}t} = \nabla \cdot \left(\frac{\nu_T}{\sigma_\varepsilon} \nabla \varepsilon \right) + C_{\varepsilon 1} \frac{P\varepsilon}{k} - C_{\varepsilon 2} \frac{\varepsilon^2}{k} \tag{2.35}$$

where ν_T is the turbulent viscosity, P is the production rate of turbulent kinetic energy and $C_\mu = 0.09$, $C_{\varepsilon 1} = 1.44$, $C_{\varepsilon 2} = 1.92$, $\sigma_\varepsilon = 1.3$ and σ_k=1.0 are model parameters [10] [14].

2.5.4 Wall Functions

In order to save computational time wall functions are often used along with the k-ε model. The wall functions are based upon the relations known from near wall flows. The near wall region can be divided into two different layers, the *viscous sublayer* and the *log-layer*. In direct proximity to the wall viscous effects are more dominant than turbulent effects. The further away from the wall the more prominent are the turbulent effects. The region where viscous effects and turbulent effects are approximately equally important is called the buffer-layer. In the log-layer the following relation is valid

$$u = u_\tau \left(\frac{1}{\kappa} ln(y^+) + B \right) \tag{2.36}$$

where

$$u_\tau = \left(\frac{\tau}{\rho}\right)^{1/2}. \tag{2.37}$$

From (2.37) the dimensionless wall distance y^+ can be constructed

$$y^+ = \frac{y\rho u_\tau}{\mu}. \tag{2.38}$$

When wall functions are used with the k-ε model the log-layer velocity profile (2.36), is applied to the mesh-node closest to the wall. For wall functions used with the k-ε model y^+ values in the range 20-100 is recommended [10] [14].

2.5.5 Free Surface Modeling

One of the most commonly used free surface model in commercial CFD codes is the volume of fluid (VOF) model. In the VOF model each element is given a volume-fraction. If that particular element is occupied by only water the volume-fraction is 1. Analogously an element occupied by only air has volume-fraction 0. In the interface between the two fluids there will be several elements that has values in the range between 0 and 1. It is common to use the volume-fraction value 0.5 to define the surface. The resolution of the mesh in proximity to the water surface is important since it directly impacts how accurate the water surface is [16].

CHAPTER 3

Method

3.1 Assumptions

Throughout this work the following assumptions have been made;

- The flow is assumed to be incompressible.
- The water surface is only subject to the atmospheric pressure.
- The k-ε model is sufficiently accurate to describe the turbulent flow properties.
- No form of temperature differences or temperature driven flow occurs.
- The flow at the inlet is entirely uniform.

3.2 Geometry

The geometry used is a channel with rough walls, the actual channel can be seen in figure 1.1. The length of the channel is 5 m, the width is 1.2 m, the radius of the corners is 0.05 m and the height is 0.7 m. The inlet and the outlet have been elongated by 0.1 m respectively, these extended parts consists of smooth walls. By extending the geometry the inlet and outlet won't be subject to steep gradients. The geometry used in the mesh-convergence study has been shortened to 1 m, however the width and height remains the same. In figure 3.1 a contour plot of the elevation along the channel bed can be seen together with the sampling planes. Some dimensions of the channel as well as the shape of the elongated inlet and outlet portions with the sampling planes can be seen in figure 3.2. The global maximum is approximately 0.27 m and the local maximum in the midplane is approximately 0.25 m.

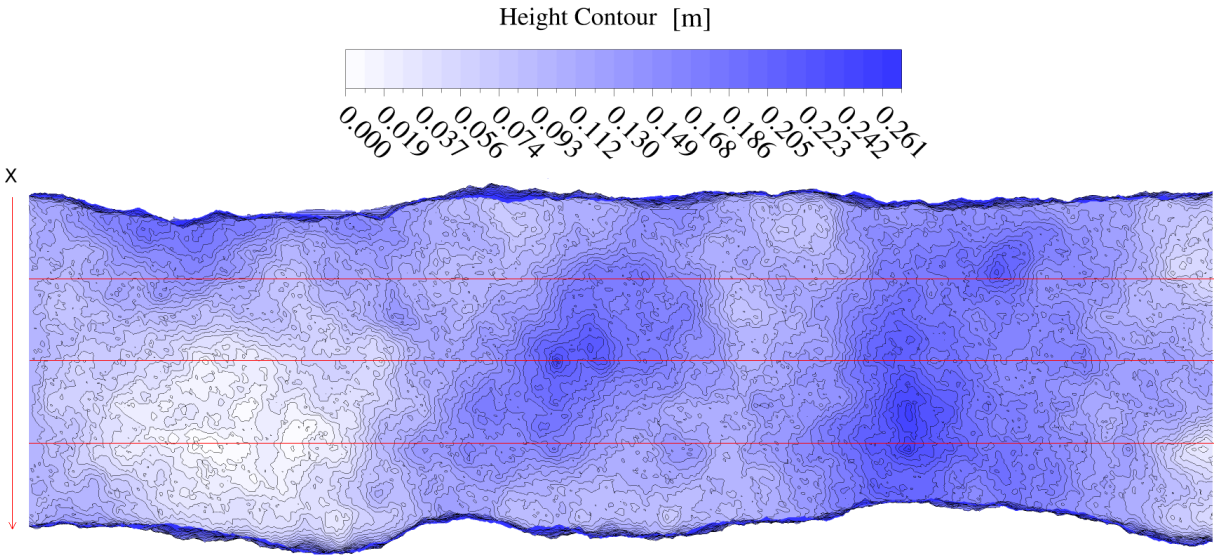

Figure 3.1: Contour plot of channel bed with three sampling planes at $x = 0.3$ m, $x = 0.6$ m and $x = 0.9$ m. The direction of the flow is from the left to the right.

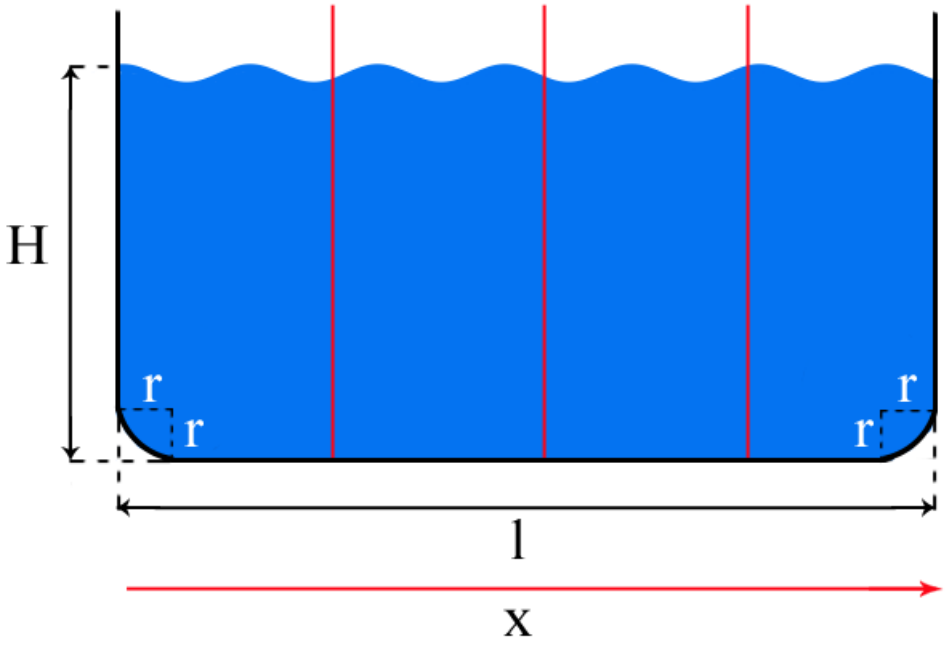

Figure 3.2: Inlet and outlet of channel with channel dimensions and three sampling planes at $x = 0.3$ m, $x = 0.6$ m and $x = 0.9$ m.

3.3 Mesh

In order to get a good representation of the chaotic rough surface an unstructured tetrahedral is used. To get good near-wall behaviour the near-wall region consists of prism elements. In figure 3.3 a cross-section for the coarsest mesh can be seen. The mesh convergence study will include five different meshes varying between 88 thousand and 1.3 million nodes. The mesh is generated in ANSYS ICEM.

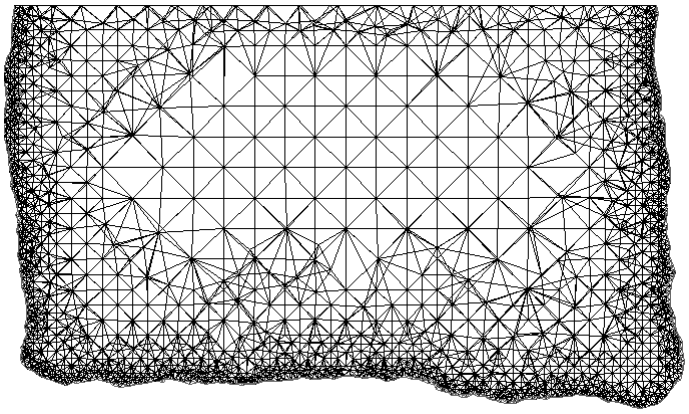

Figure 3.3: Cross-section of unstructured tetra mesh.

3.4 Simulation Setup

3.4.1 Boundary Conditions

The following boundary conditions are chosen in ANSYS CFX-Pre.

- The inlet is set as the 'inlet' condition with a turbulent intensity of 5%.
- The outlet is set as the 'opening' condition with a zero-gradient volume-fraction condition and a relative pressure set to $p_{rel} = \rho_{water} y g$ where g is the gravity and y varies linearly from 0 to the water surface height.
- The rough-walls are set to the 'no-slip wall' condition.
- The smooth walls are set to the 'no-slip wall' condition.
- Rather than using the 'opening' condition at the top of the channel a free-slip lid is introduced. This is purely because of convergence reasons.

3.4.2 Multiphase

There are two different species present in the domain, water and air. The material properties can be seen in table 3.1.

	Water	Air
Phase	Liquid	Gas
Dynamic Viscosity μ [kg/(m·s)]	1×10^{-3}	1.83×10^{-5}
Density ρ [kg/m^3]	998	1.225

Table 3.1: Species properties.

In ANSYS CFX-Pre the multiphase model used is the homogeneous model and the free surface model used is the standard model [17]. Additionally gravitational body forces are present with a downwards gravitational acceleration of 9.81 m/s^2.

3.4.3 Mesh Convergence Study Setup

The inlet velocity is set to 2 m/s. The distance from the average bed to the water-surface is set to 0.6 m. The initial velocity in the domain is set to 2 m/s. The simulation time is set to 1 s with a timestep of 0.01 s so that a fluid particle entering the domain at $t = 0$ s will have time to travel through the entire domain. The solution is considered converged once the RMS-residuals reaches 1×10^{-5}. The Richardson Extrapolation will be done using the double-averaged velocity profile. The extrapolation will be done in 45 points. The velocity profile is sampled in the midplane of the channel. The time-averaging is done in ANSYS CFX and the spatial-averaging is done in an external MATLAB script (see Appendix B). Statistics regarding the meshes used in the mesh study can be seen in table 3.2.

Number of Elements	Number of Nodes
430593	88117
985224	199872
2026205	410118
4617695	827183
6248434	1261550

Table 3.2: Mesh statistics for the mesh convergence study.

3.4.4 Full Scale Setup

The pump at Vattenfall Älvkarleby Research and Development is only capable of delivering a volume flow of Q=100 l/s. By dimensional analysis it is given that by dividing the volume flow with the cross-section area (below the water surface) of the inlet, the velocity of the inlet is obtained

$$u_{inlet} = \frac{Q}{A_c}. \tag{3.1}$$

Given the simple geometry of the inlet the cross section area below the water surface can readily be evaluated with the formula

$$A_c = l(H - r) + r(l - 2r) + \frac{\pi r^2}{2} \tag{3.2}$$

where l is the width of the inlet, H is the height of the water surface and r is the radius of the corners, see figure 3.2. Since there are two phases present in the inlet, the velocity is multiplied by a step function so that the water is the only phase in motion. (3.2) in (3.1) with a step function yields

$$u_{inlet} = \left(\frac{Q}{l(H - r) + r(l - 2r) + \frac{\pi r^2}{2}} \right) \text{step}(H - y). \tag{3.3}$$

The initial velocity in the domain is set to u_{inlet} and the initial water surface height is set to H. The full scale mesh consists of approximately ten million elements. The simulation time is set to 25 s with a time step of 0.01 s. The solution is considered converged once the RMS-residuals reaches 1×10^{-5}.

3.5 Varying the Height of the Water Surface

The flow will be simulated for four different heights of the water surface, 0.6 m, 0.5 m, 0.4 m and 0.3 m. In order to have dynamically equable flow properties the Froude number is used as a scaling parameter for the inlet condition. With $L_c = D_H$ and the values in table 3.3 the Froude number is 0.0395.

$H[m]$	$u_{inlet}[m/s]$	$Q[m^3/s]$
0.6	0.1391	0.1
0.5	0.1329	0.0796
0.4	0.1249	0.0598
0.3	0.1145	0.0411

Table 3.3: Inlet properties for the different simulations.

3.6 Procedure

3.6.1 Double-Averaging

The problem is fundamentally unsteady, in order to get meaningful and easy to interpret results the velocity field will be averaged in both space and time rather than just in time. The velocity field is time-averaged in CFX. The time averaging is started once the initial transient behaviour has passed and all that remains are phenomena due to the geometry. The velocity field is then spatially averaged in an external MATLAB script, see Appendix C. The double-averaging will be performed in three planes, see figure 3.2.

3.6.2 Gauckler-Manning Coefficient

To evaluate the Gauckler-Manning coefficient (2.21), the wall shear stress, the hydraulic radius and the average velocity are required. These variables will be evaluated in 50 cross-sectional planes equally spaced along the channel. The average velocity and the wall shear stress can be extracted directly from the CFD-Post built in functionality. The hydraulic radius, however needs to be handled externally since the cross section area and the wetted perimeter varies with the streamwise coordinate. By using CFD-Post functionality the length of the perimeter and the shape of the water surface can be determined. There is unfortunately no functionality to form a union between the two directly in CFD-Post. Instead this will be done in MATLAB, see Appendix D. Once the wetted perimeter is known the Reynolds number (with lengthscale R_H), the friction factor and the equivalent sand-grain roughness can all be evaluated.

3.6.3 Turbulent Energy Spectra

The turbulent energy spectrum function (2.5) is dependent only on the turbulent eddy dissipation ε and the turbulent kinetic energy k. By creating an iso-volume in CFD-Post for the volume beneath the water surface the average turbulent eddy dissipation and the average turbulent kinetic energy can be extracted from the built in CFD-Post functionality.

3.7 Mesh Convergence

In figure 3.4 the double-averaged velocity profile for the three finest meshes have been plotted. As can be seen there is no real difference between the different meshes, as a result of this the element size used in the 2M mesh will be used for the full scale simulations. The double-averaged velocity profile of the three coarsest meshes with errorbars based on the GCI (2.30) of the three finest meshes have been plotted in figure 3.5. The biggest uncertainty is 70.1 % at y $\approx$ 0.8. This corresponds to a velocity of 0.0103 m/s in

that specific point. The average rate of convergence $p_{average}$ was 1.8238. Oscillatory convergence ($\varepsilon_{32}/\varepsilon_{21} < 0$) was obtained in 55.56 % (25 of 45) of the points in figures 3.5-3.6.

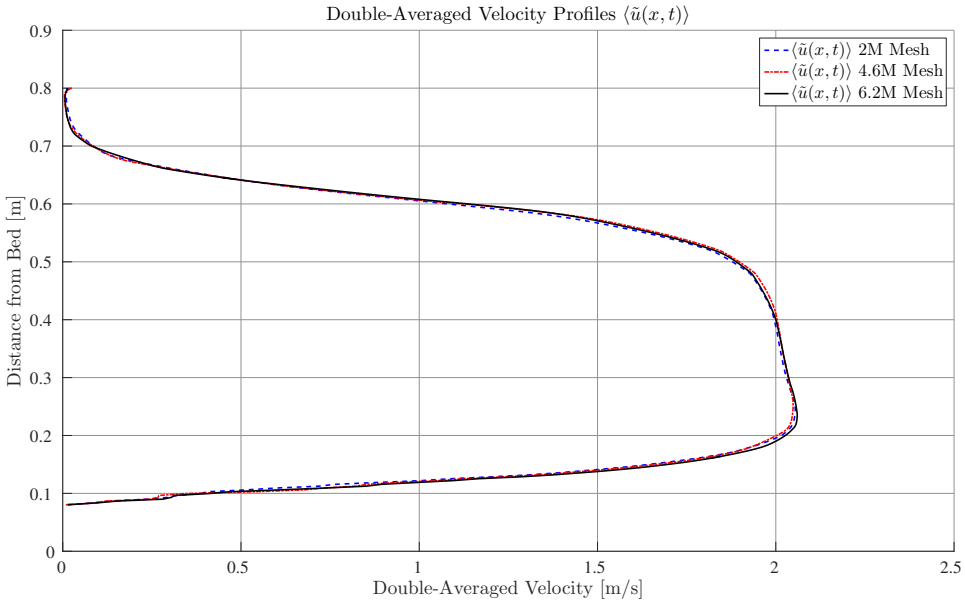

Figure 3.4: Double-Averaged velocity profile for the three finest meshes.

The errorbars based on e_{ext}^{32} (2.29) and e_a^{32} (2.28) have been plotted together with the double-averaged velocity profile for the 2M mesh in figure. 3.6. In table. 3.4 some mesh uncertainties can be seen.

	e_a	e_{ext}	GCI_{fine}
Greatest uncertainty percentage	41.62%	87.43%	70.1%
Gretest uncertainty velocity [m/s]	0.0051	0.0107	0.0103

Table 3.4: Computed errors and uncertainties.

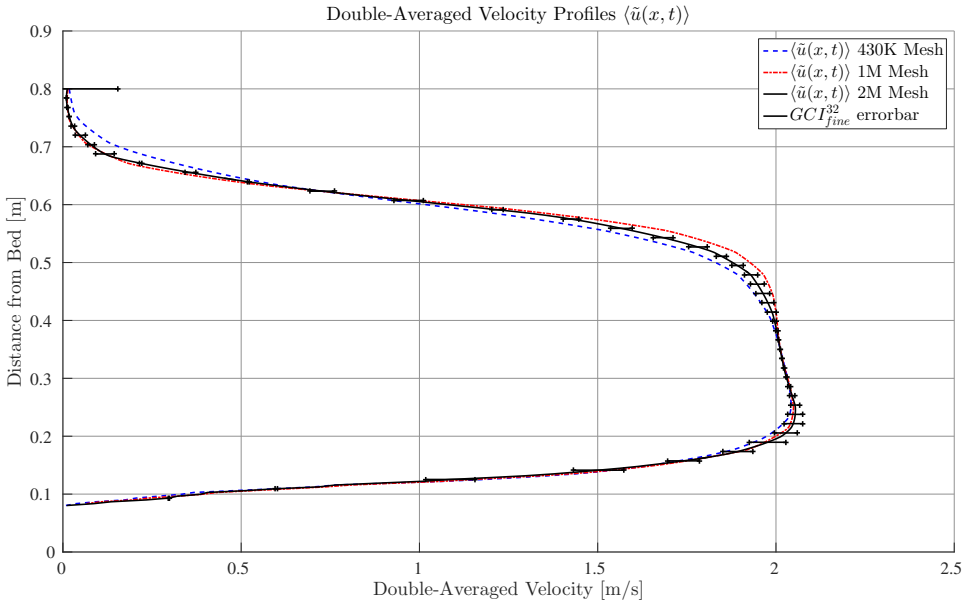

Figure 3.5: Double-Averaged velocity profile for the three coarsest meshes including errorbars from the GCI of the three finest meshes.

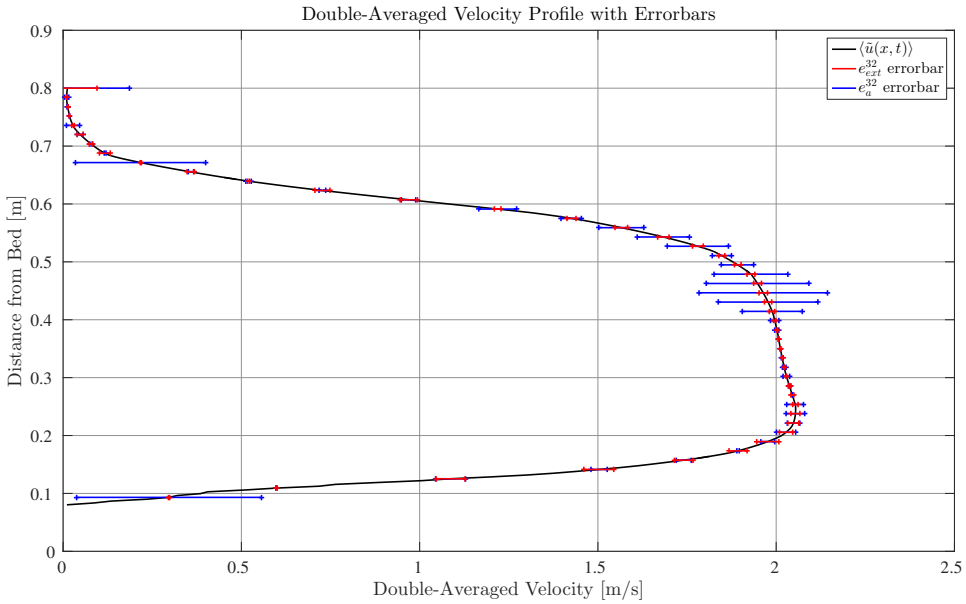

Figure 3.6: Double-Averaged velocity profile for the 2M meshes including errorbars from e^{32}_{ext} (red) and e^{32}_{a} (blue) based on the three finest meshes.

CHAPTER 4

Results

4.1 Double-Average Velocity Profiles

The double-averaged velocity profiles for the four different water levels have been plotted in figures 4.1-4.4. In each plot the double-averaged velocity profile have been sampled in three planes (see figure 3.2). The y-axes have been normalized with the water surface height H for that specific plot. This means that the y-axis will always be in the range between 0 and 1 where 0 is the bed and 1 is the level of the water surface.

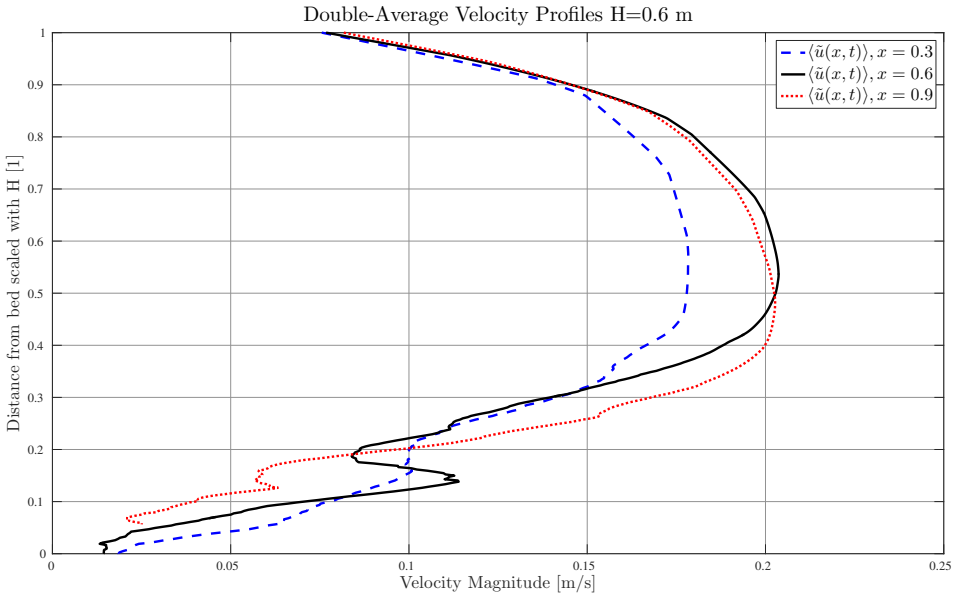

Figure 4.1: Double-average velocity profiles for the three different sampling planes for H=0.6 m.

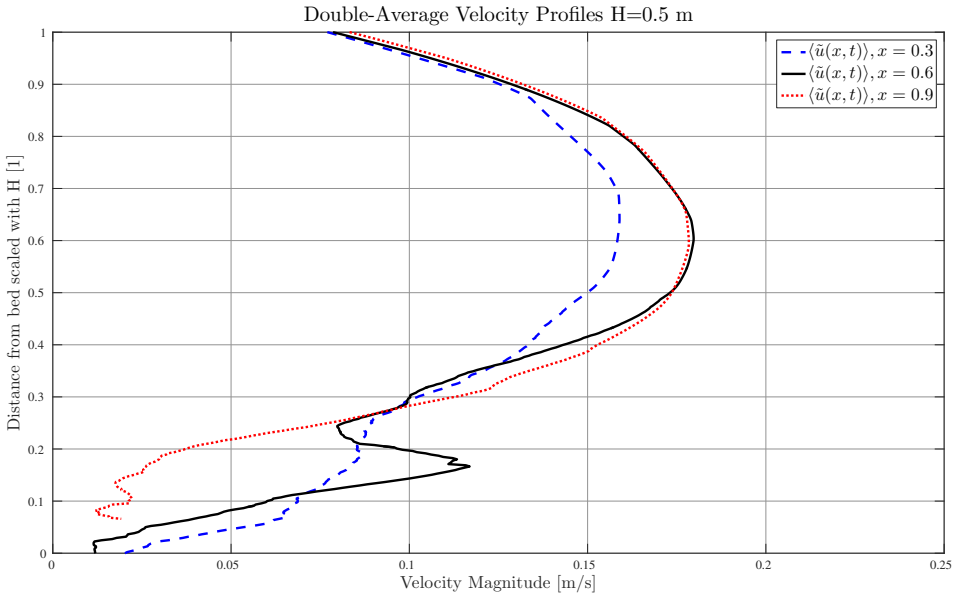

Figure 4.2: Double-average velocity profiles for the three different sampling planes for H=0.5 m.

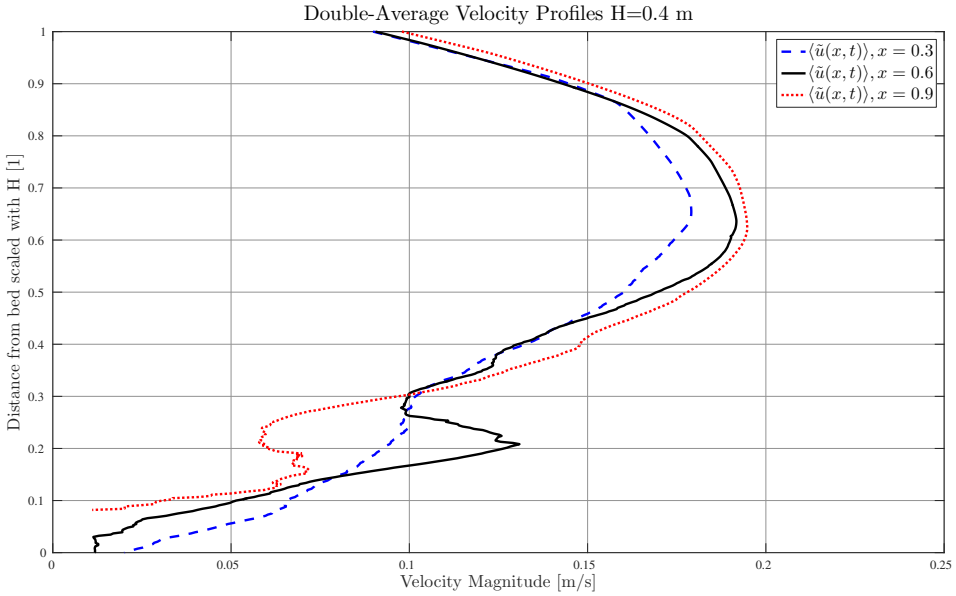

Figure 4.3: Double-average velocity profiles for the three different sampling planes for H=0.4 m.

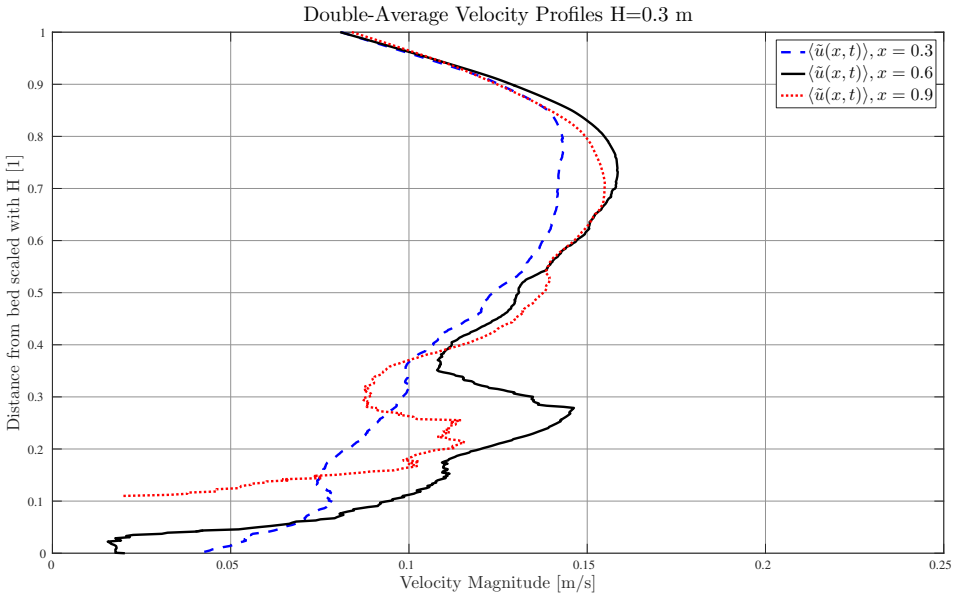

Figure 4.4: Double-average velocity profiles for the three different sampling planes for H=0.3 m.

The general shape of the curves are maintained throughout the different cases, however the proportions differs from case to case. In figure 4.1 there is a prominent peak at y≈ 0.17 for the midplane profile (black line). The magnitude of the peak is increasing as the water level is decreasing. In figure 4.1 the quota between the smaller peak and the bulk flow peak is 0.5594. For the cases where the water level is 0.5 m, 0.4 m and 0.3 m the quotas are 0.6505, 0.6827 and 0.9231 respectively. A similar peak can also be observed in the x=0.9 m plane. The peak is almost negligible in figure. 4.1 and figure. 4.2 but becomes more prominent in figures 4.3 and 4.4.

4.2 Gauckler-Manning Coefficients

In figures 4.5-4.8 the local Gauckler-Manning number has been plotted together with the average Gauckler-Manning number. The average Gauckler-Manning is 0.0157 for the case where the water level is 0.6 m. The average Gauckler-Manning number is 0.0179, 0.185 and 0.0172 for the cases where the water level is 0.5 m, 0.4 m and 0.3 m respectively. The shape of the local Gauckler-Mannings number varies between the cases. In figure 4.6 and figure 4.7 the shape is rather similar while the shape in figure 4.5 and figure 4.8 are more standalone.

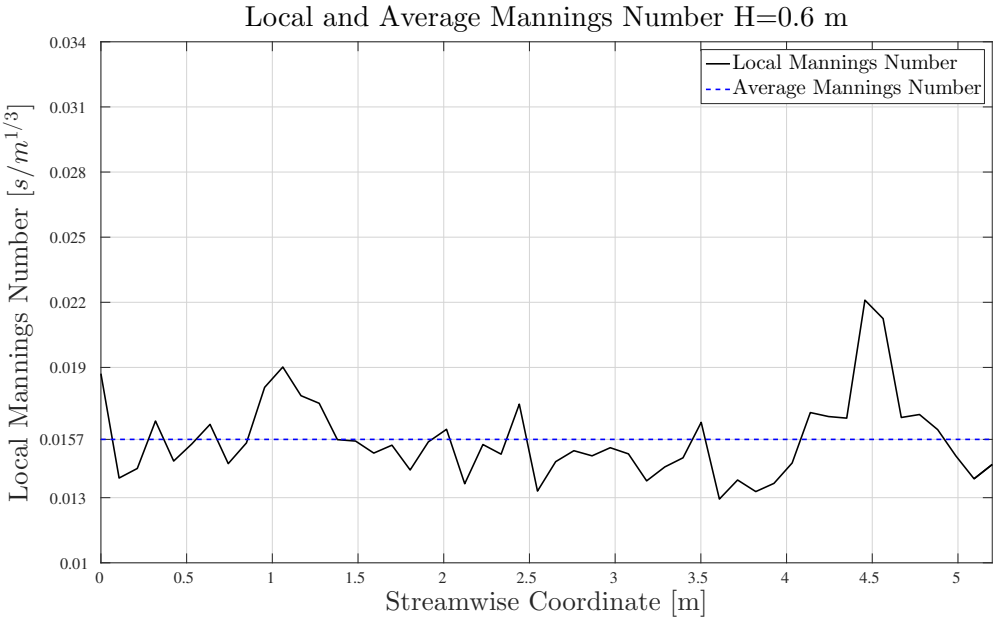

Figure 4.5: Local and average Gauckler-Mannings number plotted for the H=0.6 m case.

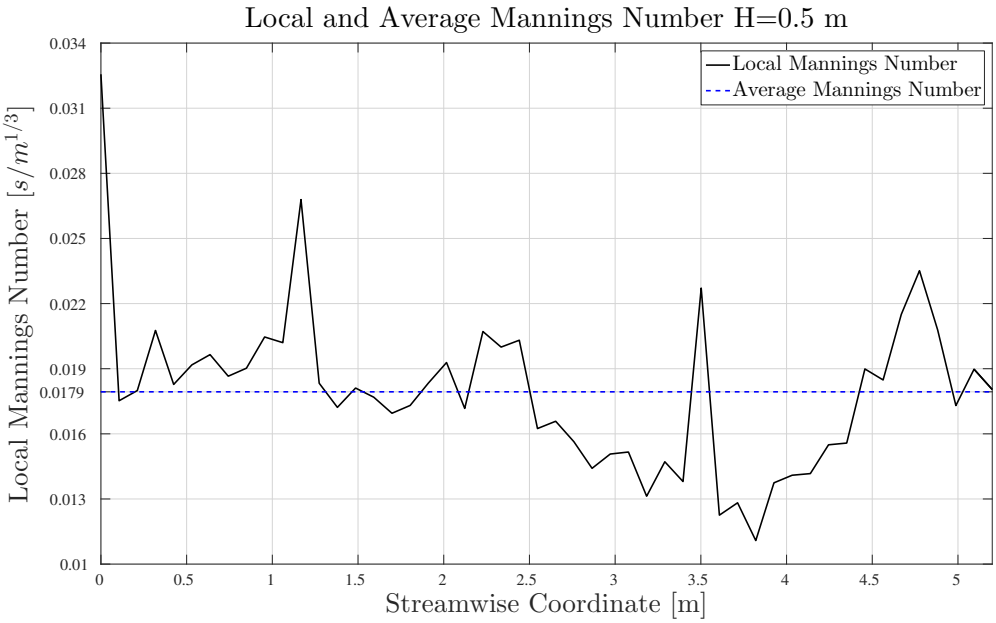

Figure 4.6: Local and average Gauckler-Mannings number plotted for the H=0.5 m case.

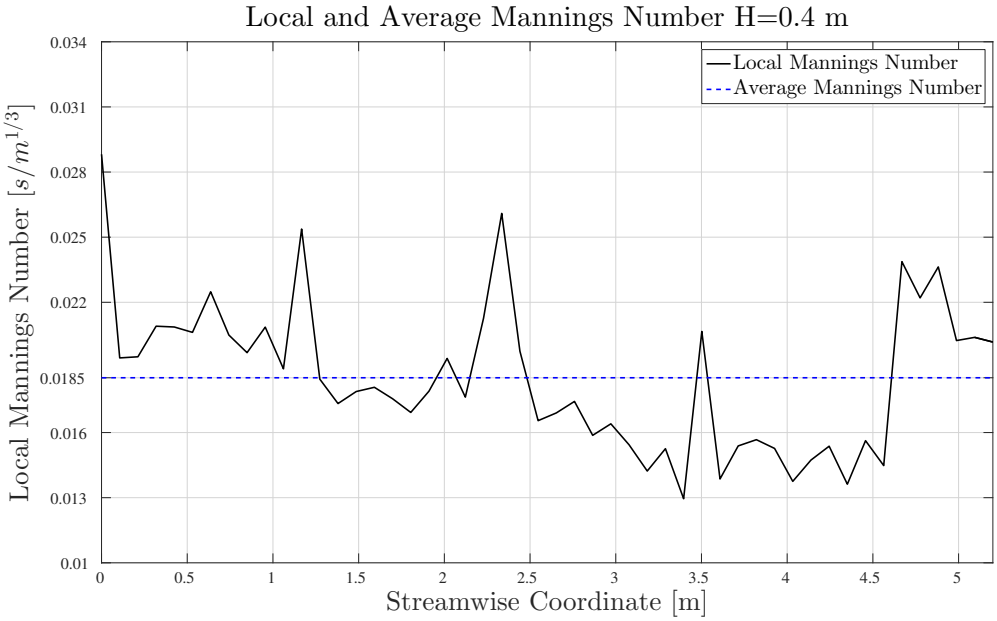

Figure 4.7: Local and average Gauckler-Mannings number plotted for the H=0.4 m case.

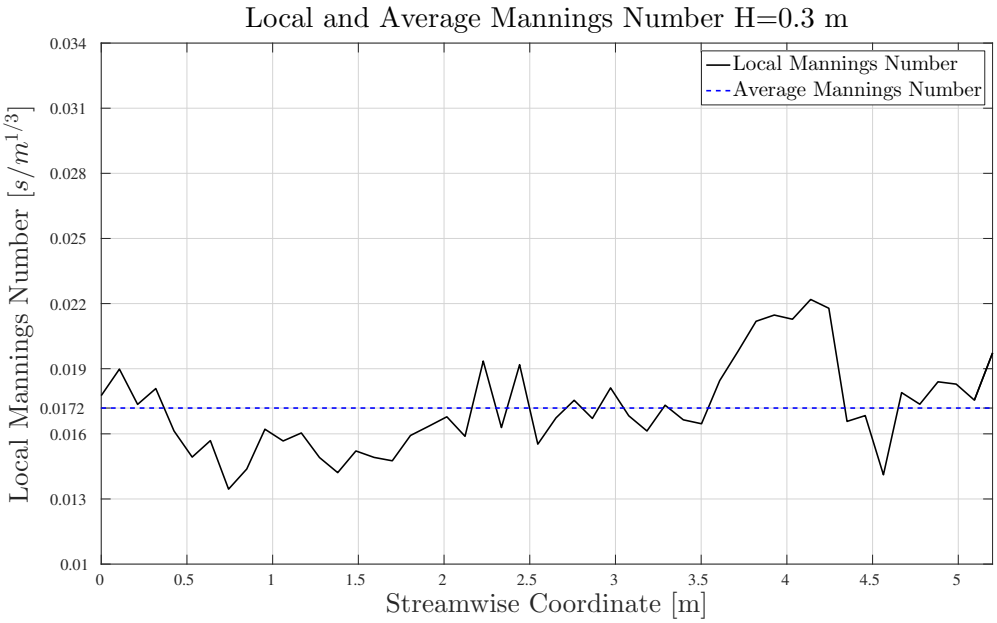

Figure 4.8: Local and average Gauckler-Mannings number plotted for the H=0.3 m case.

Derived geometrical properties have been tabulated in table 4.1. The values of f have been computed from (2.19) and the values for ϵ/R_H have been computed using (2.14).

$H[m]$	n_{mean}	f	ϵ/R_H
0.6	0.0157	0.0169	6.5×10^{-3}
0.5	0.0179	0.0290	4.4×10^{-3}
0.4	0.0185	0.0346	1.9×10^{-3}
0.3	0.0172	0.0330	3.7×10^{-3}

Table 4.1: Geometrical properties for different values of H.

4.3 Turbulent Energy Spectra

The energy spectrum function (2.5) has been made non-dimensional and plotted for five different cases in figure 4.9. The blue, brown, black and red line each correspond to different water level cases. The green line is the energy spectrum for a simulation where the equivalent sand-grain roughness applied to a smooth geometry was used instead of the rough geometry. The equivalent sand-grain roughness used was based on the case where the water level was 0.6 m ($\epsilon/R_H = 6.5 \times 10^{-3}$). In table 4.2 several turbulence properties have been tabulated for simplicity.

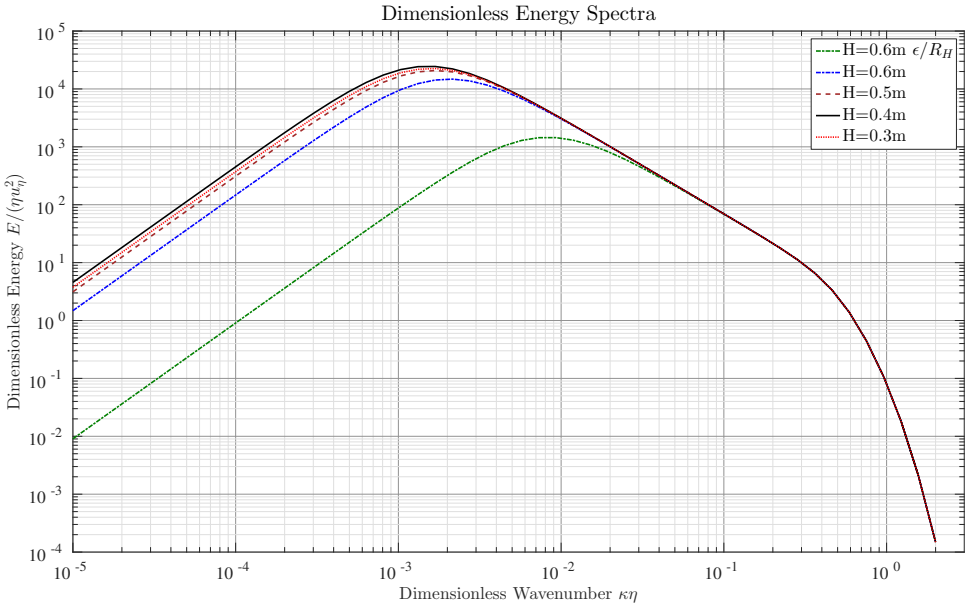

Figure 4.9: Turbulent energy spectrum for the different cases.

$H[m]$	$(E/(\kappa u_\eta^2))_{max}$	$(\kappa\eta)_{max}$	L_{max}
0.6	1.4794×10^4	2×10^{-3}	0.4288
0.5	2.0805×10^4	1.7×10^{-3}	0.5770
0.4	2.4682×10^4	1.5×10^{-3}	0.5369
0.3	2.2606×10^4	1.6×10^{-3}	0.4398

Table 4.2: Turbulent energy properties for different values of H, including corresponding most energetic lengthscale L_{max}.

4.4 Velocity Contours

The midplane, time-averaged velocity contours for the different water levels have been plotted in figures 4.10-4.13. The contours have been normalized with the maximum velocity of the contour. The contours in figures 4.10-4.12 all show the same tendency; the water surface is constant, there is zones of recirculation along the entire channel bed and there are two clear velocity maxima, one related to the local (roughness) maxima in the midplane (upstream velocity maxima from now on) and one related to the global maxima (downstream velocity maxima from now on). In figure 4.13 the upstream maxima and downstream maxima still remains and so do recirculation zones along the bed. The difference is that the water surface is no longer constant, it drops after both velocity maxima.

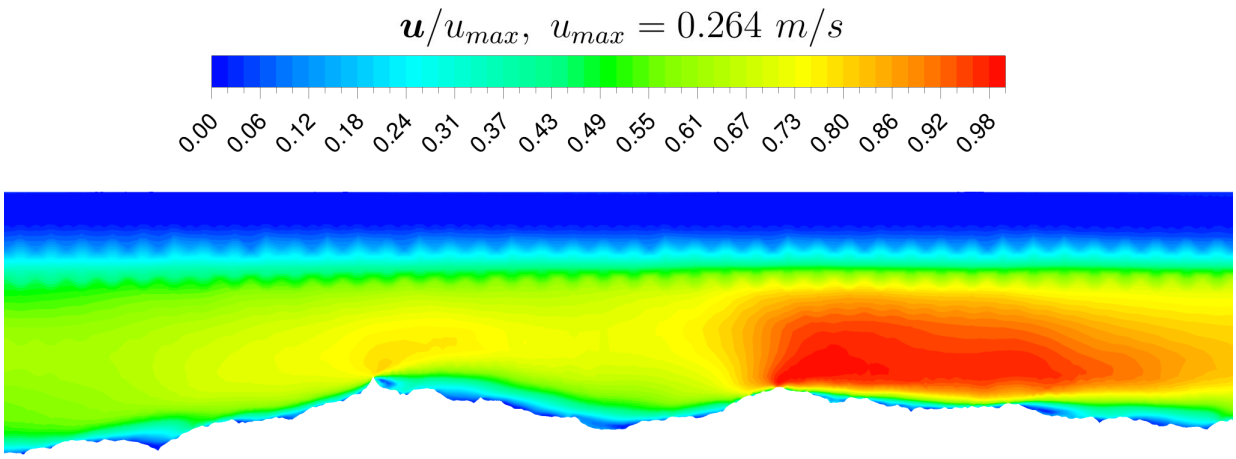

Figure 4.10: Normalized velocity contour for H=0.6 m where $u_{max} = 0.264\ m/s$.

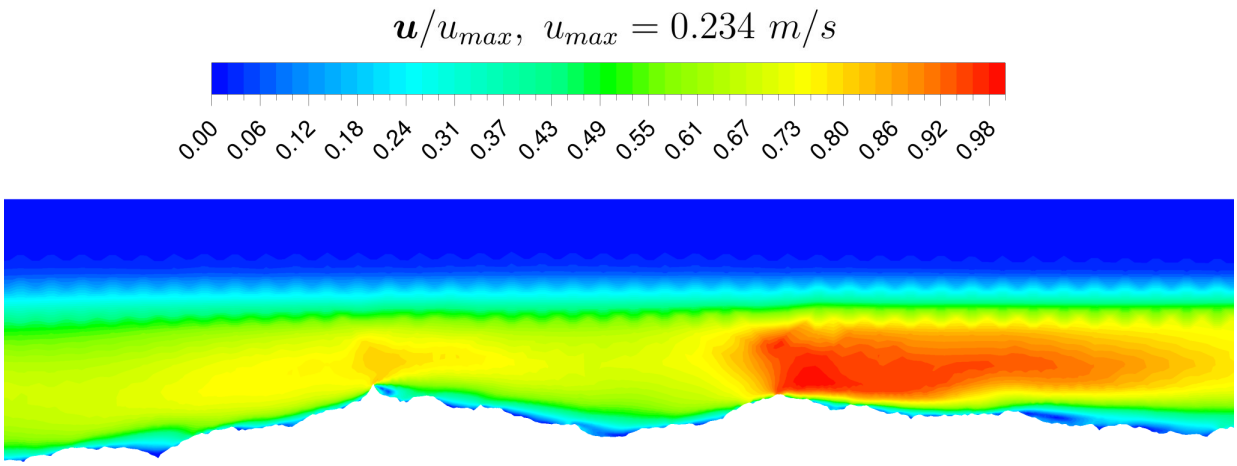

Figure 4.11: Normalized velocity contour for H=0.5 m where $u_{max} = 0.234\ m/s$.

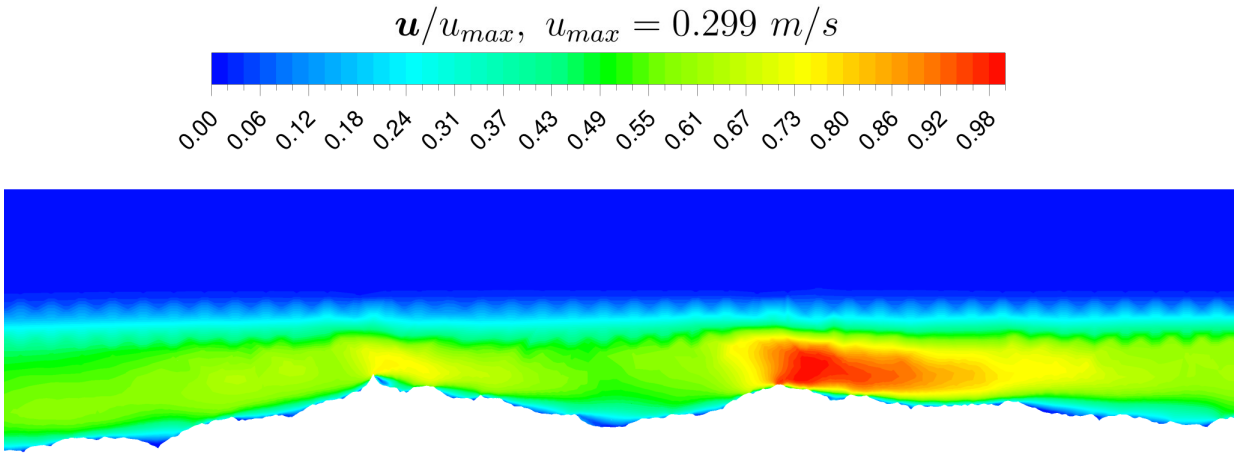

Figure 4.12: Normalized velocity contour for H=0.4 m where $u_{max} = 0.299\ m/s$.

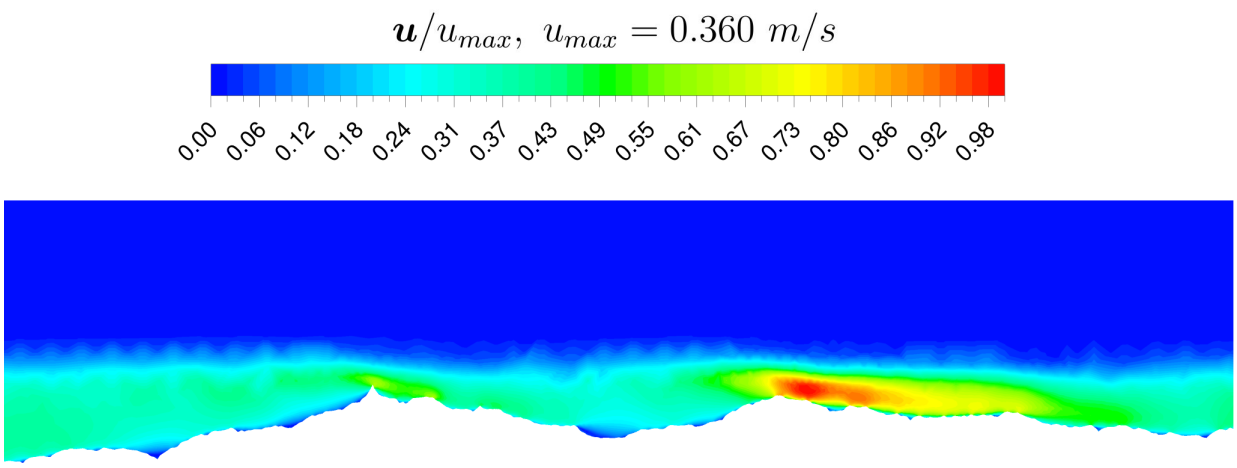

Figure 4.13: Normalized velocity contour for H=0.3 m where $u_{max} = 0.360\ m/s$.

In figures 4.14-4.17 the normalized time-averaged velocity contours have been plotted in a plane just above the global roughness maxima for the different cases. In figure 4.14 and figure 4.15 the global roughness maxima relates to the local minima in close proximity to the global velocity maxima. In a similar way the local midplane roughness maxima can be located a bit further upstream. Flow recirculation occurs along the channel walls in a similar fashion to the channel bed. In figures 4.16-4.17 the maximum velocity is closer to channel wall compared to figures 4.14-4.15, the recirculation is still apparent.

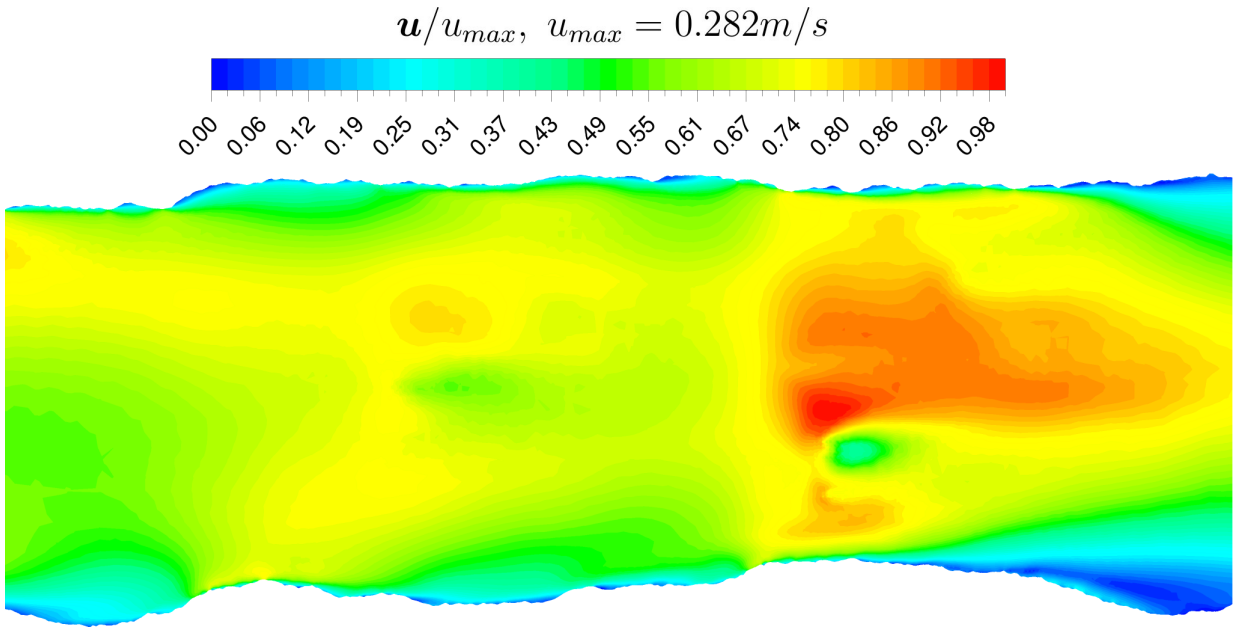

Figure 4.14: Normalized time-averaged velocity contour for H=0.6 m where $u_{max} = 0.282$ *m/s.*

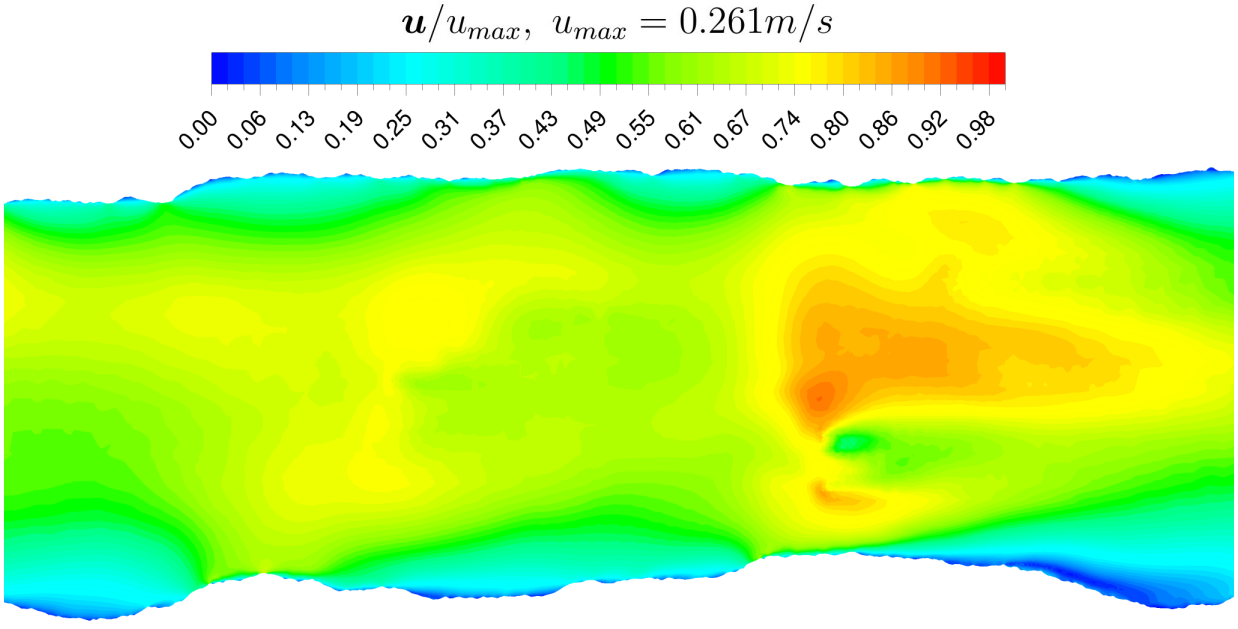

Figure 4.15: Normalized time-averaged velocity contour for H=0.5 m where $u_{max} = 0.261$ *m/s.*

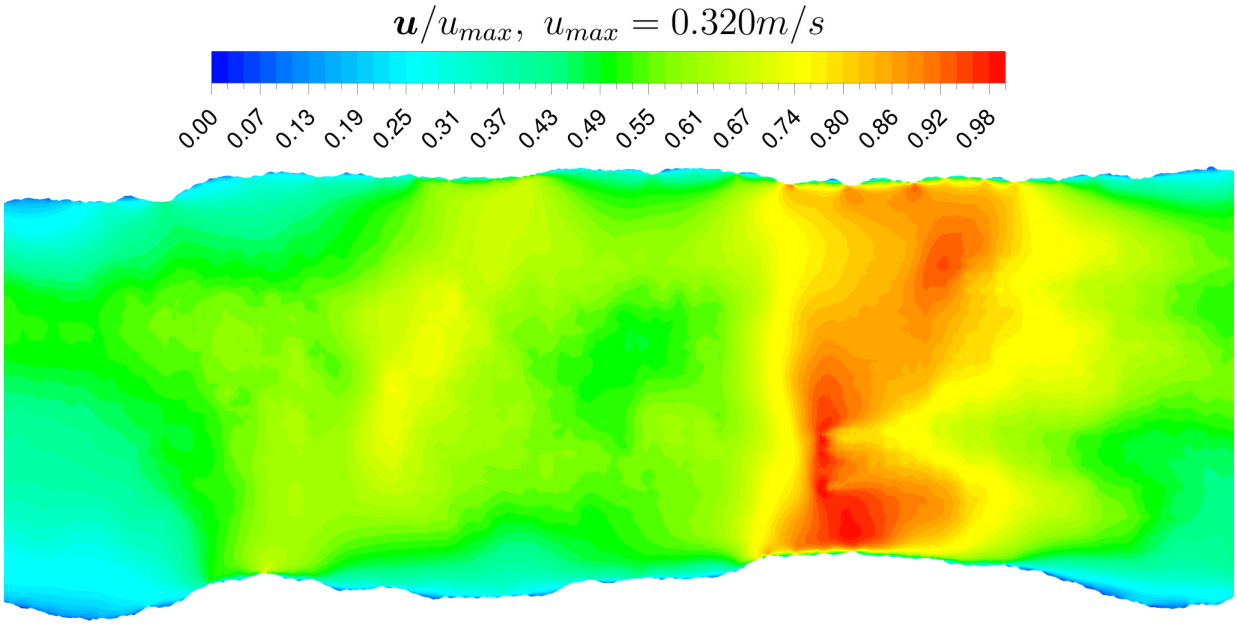

Figure 4.16: Normalized time-averaged velocity contour for H=0.4 m where $u_{max} = 0.320$ *m/s.*

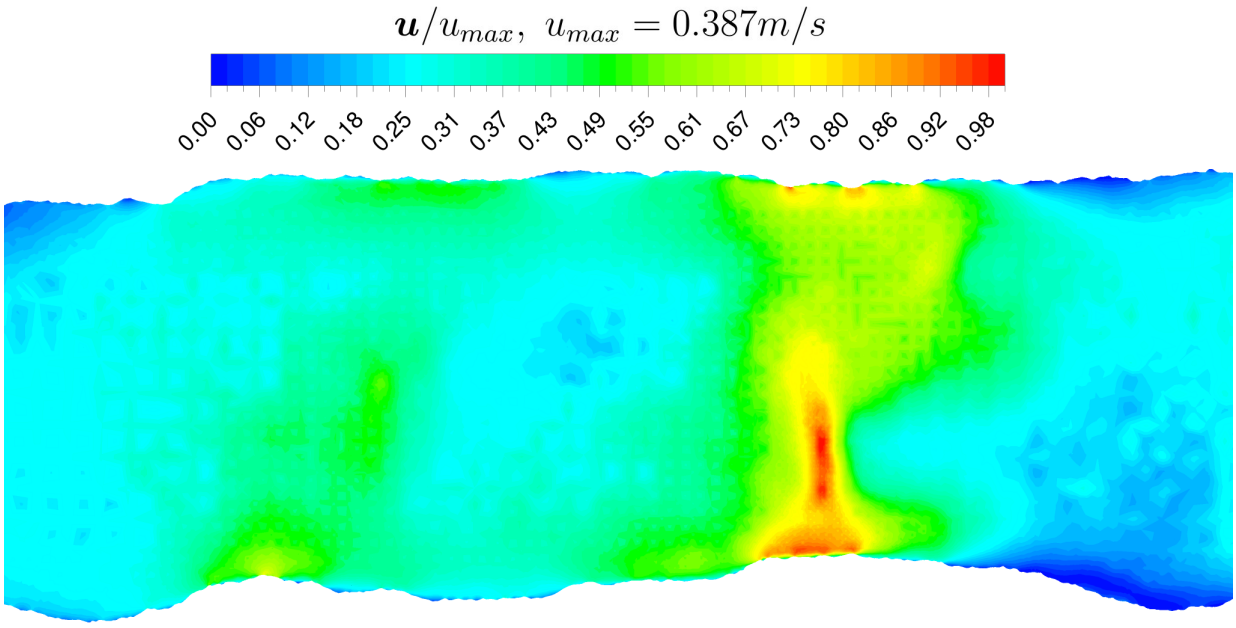

Figure 4.17: Normalized time-averaged velocity contour for H=0.3 m where $u_{max} = 0.3870$ *m/s.*

In figures 4.18-4.19 the normalized, time-averaged velocity contours have been plotted in the cross-section plane that intersects the global roughness maxima. In figure 4.18 the velocity maxima is close to the centre for both cases, however for the H=0.5 m case there are higher velocities close to the left corner. This trend is continued further in figure 4.19 where the global maxima is in the left corner for both cases. The shape of the water surface is the same for all cases except the H=0.3 m case where a depression can be seen close to the roughness maxima.

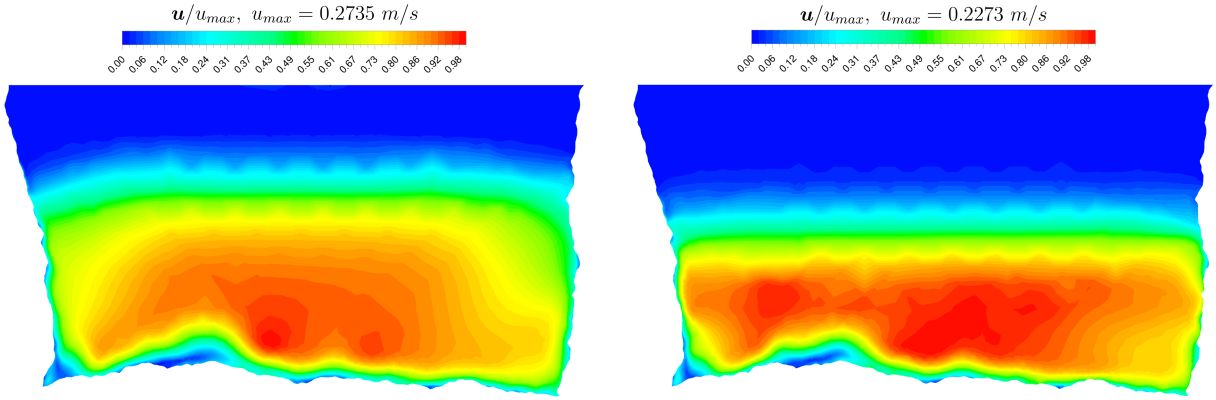

Figure 4.18: Normalized time-averaged velocity contours for H=0.6 m (left) and H=0.5 m (right) where $u_{max} = 0.2735\ m/s$ *and* $u_{max} = 0.2273$ *respectively.*

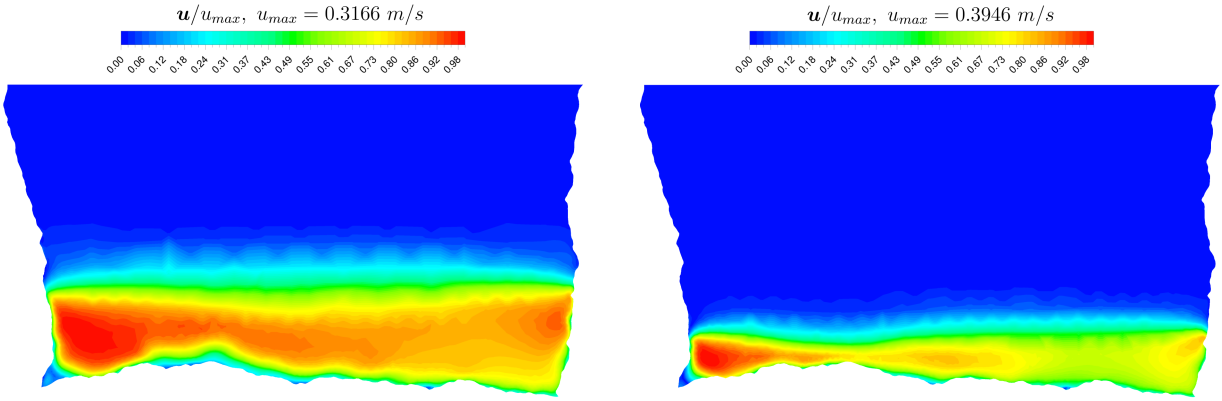

Figure 4.19: Normalized time-averaged velocity contours for H=0.4 m (left) and H=0.3 m (right) where $u_{max} = 0.3166\ m/s$ *and* $u_{max} = 0.3946\ m/s$ *respectively.*

CHAPTER 5

Discussion and Conclusions

5.1 Discussion

Regarding the shape of the double-average velocity profiles (figures 4.1-4.4), the red and black lines are sampled in two planes where there are prominent roughness elements. This in turn might make the magnitude of the peak skewed towards a higher velocity peak. The blue line is sampled in a plane where the roughness is not as dramatic, this is reflected in the shape where the shape is more constant than in the other two cases. It is possible that for an infinitely long channel the red and black line will approach the shape of the blue line since the fractal algorithm used to generate the roughness is based on a Gaussian distribution.

As for the Gauckler-Manning coefficients (figures 4.5-4.8 and table 4.1), they range from 0.0157-0.0185. This approximately corresponds to the value of asphalt in table 5.1.

Wall Material	n
Glass	0.010
Smooth Steel	0.012
Finished Concrete	0.012
Unfinished Concrete	0.014
Asphalt	0.016
Clean Excavated Earth Channel	0.022
Gravelly Excavated Earth Channel	0.025
Clean Natural Channel	0.030
Mountain Streams	0.050

Table 5.1: Tabulated values of Gauckler-Mannings coefficients for different channels [18].

The values for the Gauckler-Manning coefficients seem to be quite low, one would expect that the channel would be comparable with natural channels or at the very least excavated channels. From (2.21) it is given that the Gauckler-Manning coefficient is a direct function of the average wall shear stress. One explanation for the low simulated Gauckler-Manning values is that the $k - \varepsilon$ model underestimates the wall shear stress. This could be because of the use of wall functions.

The equivalent sand-grain roughness ϵ/R_H is at its largest for the smallest friction factor f. The reason for this is because the equation (2.14) is also a function of the Reynolds number, thus there is no one-to-one relation between the equivalent sand-grain roughness and the friction factor f since the Reynolds number is different in every simulation.

Concerning the turbulent energy spectra (figure 4.9) experiments needs to be made in order to validate which model describes the energy spectra best.

While the general trend for the velocity contours taken in the midplane (figure 4.10-4.13) is similar the same can't be said for the remaining contours. The behaviour of the flow in figures 4.14-4.17 is apparent first when viewed together with figures 4.18-4.19. The sampling plane is so close to the bed, that some of the higher velocities in figure 4.18 are missed in figure 4.14. From figures 4.18-4.19 it can also clearly be seen that the lower water level forces the water to take other ways than for higher water levels. This means that the higher velocities will be closer to the channel bed, this behaviour is captured in figures 4.16-4.17. The apparent diffusion that can be seen in figure 4.17 is the water surface that intersects the sampling plane.

5.2 Conclusions

In this thesis several properties of a rough surface channel have been presented. The double-average velocity profile for several different water levels have been evaluated, as well as the turbulent energy spectra and the Gauckler-Manning coefficient for the channel has been determined from CFD simulations. Several velocity contours have been provided to visualize the flow. The rough geometry gives rise to flow separation along the channel bed and walls. The rough geometry can also be related to areas of high flow velocity. It has also been shown that the water level greatly affects the flow field. As a complement to the Gauckler-Manning coefficients, the friction factor f and the equivalent sand-grain roughness ϵ/R_H have been provided for all different cases. This work clearly demonstrates the need to resolve the actual roughness and not using sub-grid methods as a model for large scale roughness. Especially for cases with biological applications such as bottom flora and fauna.

5.3 Future Work

This thesis is a good initial study regarding properties of open-channel flow over rough surfaces, however there is room for further studies.

- This work is purely based on CFD, just as any other CFD case it needs to be validated with real world experiments.
- The k-ε model is probably insufficient to properly describe the near-wall behaviour of the flow. A similar study but with a more advanced turbulence model, i.e a k-ω model, a SST model, LES or a Reynold Stress Model would be very interesting.
- Simulations on a similar, longer channel would also be of interest. In this work the channel could'nt be any longer since the simulations would take too long.
- Simulations with even lower water levels, where some roughness elements are exposed, are also of additional interest.
- Sediment transport in the channel could be of additional interest as well.
- Biological applications such as influence on flora and fauna.

CHAPTER 6

Bibliography

[1] Svensk Energi. Elåret 2014, May 2015. URL http://www.svenskenergi.se/Global/Statistik/El%C3%A5ret/El%C3%A5ret%202014_slututg%C3%A5va.pdf.

[2] Länsstyrelsen. Vandringshinder för djur i vattendrag, 2005. URL http://web.archive.org/web/20051231071534/http://www.ab.lst.se/upload/dokument/publikationer/M/Rapportserien/2005/R2005_22_Vagtrummor_o_dammar_webb.pdf.

[3] EUR-Lex. Good-quality water in europe (eu water directive), July 2015. URL http://eur-lex.europa.eu/legal-content/EN-SV/TXT/?qid=1459247104762&uri=URISERV:l28002b&from=EN.

[4] S Nakagawa, Y Na, and TJ Hanratty. Influence of a wavy boundary on turbulence. *Experiments in Fluids*, 35(5):422–436, 2003.

[5] Dubravka Pokrajac, Lorna Jane Campbell, Vladimir Nikora, Costantino Manes, and Ian McEwan. Quadrant analysis of persistent spatial velocity perturbations over square-bar roughness. *Experiments in fluids*, 42(3):413–423, 2007.

[6] Anders Andersson. *Modelling flow with free and rough surfaces in the vicinity of hydropower plants*. PhD thesis, Luleå University of Technology, 2013.

[7] Joel H Ferziger and Milovan Peric. *Computational methods for fluid dynamics*. Springer Science & Business Media, 2012.

[8] Yunus A Çengel and Cimbala. *Fluid mechanics fundamentals and applications*. Tata McGraw-Hill Education, 2014.

[9] U Frisch. *Turbulence: the legacy of A. N. Kolmogorov*. Cambridge University Press, 1995.

[10] Stephen B Pope. *Turbulent flows*. Cambridge University Press, 2000.

[11] Alain Fournier, Don Fussell, and Loren Carpenter. Computer rendering of stochastic models. *Communications of the ACM*, 25(6):371–384, 1982.

[12] Vladimir Nikora, Stephen McLean, Stephen Coleman, Dubravka Pokrajac, Ian McEwan, Lorna Campbell, Jochen Aberle, Dougal Clunie, and Katinka Koll. Double-averaging concept for rough-bed open-channel and overland flows: Applications. *Journal of hydraulic Engineering*, 133(8):884–895, 2007.

[13] Hubert Chanson. *Hydraulics of open channel flow*. Butterworth-Heinemann, 2004.

[14] Michael Casey, Torsten Wintergerste, and Sulzer Innotec. Ercoftac special interest group on quality and trust in industrial cfd. *Best practice guidelines*, 2000.

[15] Ishmail B Celik, Urmila Ghia, Patrick J Roache, et al. Procedure for estimation and reporting of uncertainty due to discretization in {CFD} applications. *Journal of fluids {Engineering-Transactions} of the {ASME}*, 130(7), 2008.

[16] Cyril W Hirt and Billy D Nichols. Volume of fluid (vof) method for the dynamics of free boundaries. *Journal of computational physics*, 39(1):201–225, 1981.

[17] ANSYS INC. Ansys 16 documentation, 2016.

[18] Ven Te Chow. *Open channel hydraulics*. McGraw-Hill Book Company, Inc; New York, 1959.

CHAPTER 7

Appendix

7.1 Appendix A - Derivation

The Colebrook equation is

$$\frac{1}{\sqrt{f}} = -2\log_{10}\left(\frac{\epsilon/D_H}{3.7} + \frac{2.51}{Re\sqrt{f}}\right). \tag{7.1}$$

Dividing by -2 yields the expression

$$\frac{-1}{2\sqrt{f}} = \log_{10}\left(\frac{\epsilon/D_H}{3.7} + \frac{2.51}{Re\sqrt{f}}\right). \tag{7.2}$$

By using the logarithmic relation that $10^{log_{10}(z)} = z$ the following is obtained

$$10^{\frac{-1}{2\sqrt{f}}} = \frac{\epsilon/D_H}{3.7} + \frac{2.51}{Re\sqrt{f}}. \tag{7.3}$$

Subtracting $\frac{2.51}{Re\sqrt{f}}$ yields

$$10^{\frac{-1}{2\sqrt{f}}} - \frac{2.51}{Re\sqrt{f}} = \frac{\epsilon/D_H}{3.7}. \tag{7.4}$$

The relation $10^{-z} = 1/10^{z}$ yields

$$\frac{1}{10^{\frac{1}{2\sqrt{f}}}} - \frac{2.51}{Re\sqrt{f}} = \frac{\epsilon/D_H}{3.7}. \tag{7.5}$$

Finally by multiplying with 3.7 the final expression is obtained as

$$\frac{\epsilon}{D_H} = 3.7\left(\frac{1}{10^{\frac{1}{2\sqrt{f}}}} - \frac{2.51}{Re\sqrt{f}}\right). \tag{7.6}$$

7.2 Appendix B - Richardson Extrapolation Function

```
function [pold, paverage, e32, e21, ea32, ea21, phi21ext, phi32ext, ...
    e21ext, e32ext, gci21, gci32]=richardsonextrapolation(phi1, phi2, phi3)
% All the definitions and notations are taken from the article 'Procedure
%for Estimation and Reporting of Uncertainty Due to Discretization in CFD
%Applications' published in Journal of Fluids Engineering July 2008.


%% Representative Mesh Size
h1=(1/2026205)*(1.28756)^(1/3); %2m
h2=(1/4617695)*(1.28756)^(1/3); %4m
h3=(1/6248434)*(1.28756)^(1/3); %6m

%% Refinement Factor
r21=h1/h2;
r32=h2/h3;

%% Differences
e32=phi3-phi2;
e21=phi2-phi1;

%% Approximation of apparent order P

f=@(p) p-(1/log(r21))*abs(log(abs(e32./e21))+...
log((r21.^p-sign(e32./e21))./(r32.^p-sign(e32./e21)))); %Extrapolation
h=1e-10; % smaller h yields better approximate derivative
derivative=@(p) (f(p+h)-f(p))/h; %Numerical derivative

% Newton-Rahpson solver
tol=1e-10; %Tolerance
pold=1.5; %Initial guess

dif=1; %Initialize loop
pnew=0;
while dif>tol
    pnew=pold-f(pold)./derivative(pold); %Newton Raphson extrapolation
    dif=abs(pnew-pold); %check if tolerance is achieved
    pold=pnew; % redefining variable for next iteration
end
paverage=mean(pold);
%% Extrapolations, Approximations and Errors
phi21ext=(r21.^pold.*phi1-phi2)./(r21.^pold-1);
phi32ext=(r32.^pold.*phi2-phi3)./(r32.^pold-1);
ea32=abs((phi2-phi3)./phi2);
ea21=abs((phi1-phi2)./phi1);
```

```
e21ext=abs((phi21ext-phi1)./(phi21ext));
e32ext=abs((phi32ext-phi2)./(phi32ext));

gci21=(1.25*ea21)/(r21.^paverage-1);
gci32=(1.25*ea32)/(r32.^paverage-1);


end
```

7.3 Appendix C - Double Averaging Function

```
function[M,t]=doubleaverage(G,h)
% This function has been created with a sample plane of 500x500 samples in
% CFD-post. If a smaller or larger sample plane is used, modifiy the factor
% 500 in the commands below.
G1=reshape(G(:,1),500,500); %Velocity Matrix

% reshape sorts the 250000 element long vector of velocity components into
% a 500x500 matrix corresponding to the domain

t=G(1:500,3); %Plot vector

M=sum(G1,2)./sum(G1~=0,2); % Averaging excluding zeros

end
```

7.4 Appendix D - Wetted Perimeter Function

```
function [Pw]=Wetted_Perimeter(X1,X2)
%This function computs the length of the wetted perimeter given a water
%surface profile (X1) and a channel cross-section (X2).

%% Loops to find the coordinates

%Iteration variables
i=1;
j=1;

%This loop finds the intersection between the water-surface and the rough
%walls from the right.
while i<length(X2)

    if round(X2(i,1),2)==round(X1(1,1),2) && ...
        round(X2(i,2),2)==round(X1(1,2),2)
        break
    end
  i=i+1;
end
%This loop finds the intersection between the water-surface and the rough
%walls from the left.
while j<length(X2)

    if round(X2(end-j,1),2)==round(X1(end,1),2) && ...
        round(X2(end-j,2),2)==round(X1(end,2),2)
        break
    end
  j=j+1;
end
X2=[X2(i:end-j,1) X2(i:end-j,2)]; %The profile under the water surface

%% Calculate the length of the wetted perimeter

i=1; %Iteration variable
l=0; %Initial length
while i<length(X2)

    ly=X2(i+1,1)-X2(i,1); %Difference in y-direction
    lx=X2(i+1,2)-X2(i,2); %Difference in x-direction
    l=l+sqrt(ly^2+lx^2); % Pythagorean theorem
i=i+1;
end
Pw=l;
end
```